JACS
JOURNAL OF THE AMERICAN CHEMICAL SOCIETY

Article

pubs.acs.org/JACS

Nonequilibrium Synthesis of Silica-Supported Magnetite Tubes and Mechanical Control of Their Magnetic Properties

Rabih Makki and Oliver Steinbock*

Department of Chemistry and Biochemistry, Florida State University, Tallahassee, Florida 32306-4390, United States

Supporting Information

ABSTRACT: Materials synthesis far from thermodynamic equilibrium can yield hierarchical order that spans from molecular to macroscopic length scales. Here we report the nonequilibrium formation of millimeter-scale iron oxide−silica tubes in experiments that tightly control the tube radius and growth speed. The experiments involve the hydrodynamic injection of an iron (II,III) solution into a large volume of solution containing sodium silicate and ammonium hydroxide. The forming tubes are pinned to a motorized glass rod that moves at a predetermined speed. X-ray diffraction and electron microscopy, as well as Raman and Mössbauer spectroscopy, reveal magnetite nanoparticles in the range of 5−15 nm. Optical data suggest that the magnetite particles follow first-order nucleation−growth kinetics. The hollow tubes exhibit superparamagnetic behavior at room temperature, with a transition to a blocked state at T_B = 95 K for an applied field of 200 Oe. Heat capacity measurements yield evidence for the Verwey transition at 20 K. Finally, we show a remarkable dependence of the tubes' magnetic properties on the speed of the pinning rod and the injection rate employed during synthesis.

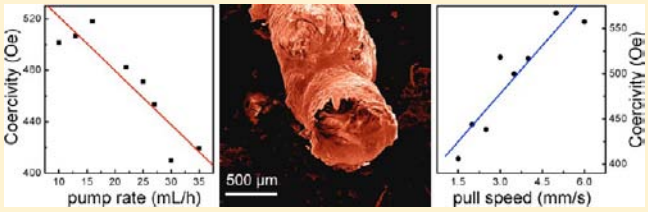

1. INTRODUCTION

Chemistry far from thermodynamic equilibrium can be expected to yield powerful tools for modern materials science. It allows the reversible or irreversible assembly of novel, hierarchically ordered structures that grow from the molecular level into macroscopic architectures.[1] In these processes, the interplay of chemical and transport phenomena facilitates the self-organization of the building blocks across multiple length-scales.[2] This synergy leads to the emergence of well-defined superstructures that can mimic biological systems or constitute unprecedented, synthetic materials. Remarkable examples include the frontal polymerization production of hydrogels,[3] the preparation of polymer composites with self-healing features,[4] as well as the formation of self-propelled structures[5] and hierarchically ordered materials.[6]

The formation of inorganic tubular structures has attracted much interest since the discovery of carbon nanotubes. Many approaches have been developed to achieve synthesis of multiscale tubes owing to their unique physicochemical properties and potential applications in many fields. In general, the formation of inorganic tubes relies mostly on template-directed growth methods.[7] Common procedures involve deposition of the precipitating material around preexisting static templates that are selectively removed via thermal or chemical treatment. Other templating strategies employ precursors that are first generated *in situ* and then act as self-sacrificing templates for the growing tubes.[8] Even other synthesis routes include rolling up layered materials[9] and hydrothermal methods.[10]

The main challenges for the use of tubular structures in materials science and engineering are twofold. The first challenge is the control of the system's large-scale features which include the creation of bifurcation points and connected networks. In this context, Cronin and co-workers recently achieved a high degree of control over tubes forming from polyoxometalate crystals immersed in dilute aqueous solutions of organic cation.[11−13] The authors demonstrated the formation of complex tubular shapes using external electric fields, local obstacles, and computer-controlled holographic heating. Branched tubular structures were also obtained by puncturing the forming tubes.[11] Chen et al. and Mohapatra et al. prepared similar Si networks and *Y*-shaped TiO_2 nantoubes using templating and sonoelectrochemical anodization methods.[14,15] The second challenge is to control the tube material itself, ideally in a spatially resolved fashion. Recent progress toward this goal yielded increased catalytic activity, specific optical features, as well as sensing abilities. For instance, work by Pagano et al. demonstrated the nonequilibrium synthesis of SiO_2-supported, photocatalytically active ZnO tubes.[16] Earlier work by Collins et al. report the production of tubular systems that are highly efficient Brønsted acid catalysts.[17] If both challenges were to be met, the resulting products would provide intricate three-dimensional networks of conduits with tailored materials characteristics.

In this work, we describe the production of silica-supported magnetic tubes. Possible target materials for such a study include magnetite (chosen here) and other metal oxides such as cobalt, nickel and manganese oxides.[18,19] We employ a method recently reported in ref 20 that physically controls the growth

Received: July 3, 2012
Published: August 15, 2012

   dx.doi.org/10.1021/ja3064843 | J. Am. Chem. Soc. 2012, 134, 15519−15527

of the millimeter-scale tubes in the reaction between nonalkali metal salt and sodium silicate solutions. Up to now, this approach had been demonstrated only for the hydrodynamic injection of copper sulfate solution.[20] The forming tubes are pinned to a motorized glass rod that directs the tube's growth. Systematic measurements showed that the velocity of the pinning rod determines the velocity of the forming tubes. Furthermore, the tube radius is selected according to volume conservation of the injected solution.[20]

In this paper, we apply these experimental principles to the synthesis of iron oxide–silica tubes and characterize the product structures using powder X-ray diffraction as well as Raman and Mössbauer spectroscopy. In addition, we analyze the growth kinetics of iron oxide nanoparticles along the forming tube. Perhaps the most interesting finding of our study is that the magnetic properties of the hollow tubes depend systematically on the speed of the pinning rod and the employed injection rate.

2. EXPERIMENTAL METHODS

2.1. Materials. The reagents used in this work are iron chloride hexahydrate ($FeCl_3 \cdot 6H_2O$, Fisher), iron chloride tetrahydrate ($FeCl_2 \cdot 4H_2O$, JT Baker), sodium meta-silicate pentahydrate ($Na_2SiO_3 \cdot 5H_2O$, Fisher), ammonium hydroxide (NH_4OH, Fisher), and magnetite powder (Fe_3O_4, Sigma-Aldrich). All chemicals are of analytical grade and solutions are prepared using nanopure water (18 MΩ cm, Easy-pure UV, Barnstead).

2.2. Synthesis. As shown in Figure 1, magnetite–silica tubes are prepared by the hydrodynamic injection of an iron (II,III) solution

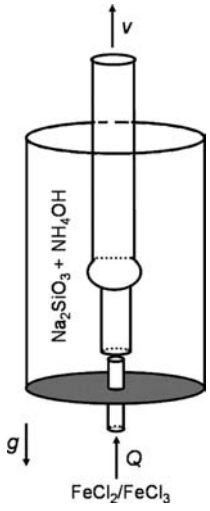

Figure 1. Schematic drawing of the experimental setup. An air-filled glass rod moves upward with a computer-controlled speed v. Attached to the bottom end of the glass rod is a large air bubble. Simultaneously, Fe(II/III) solution is injected at a constant pump rate Q into a large reservoir containing a silicate–ammonia solution. The vector g denotes gravity.

([Fe(III)]/[Fe(II)] = 2:1) into a large reservoir (approximately 60 mL) of sodium silicate and ammonium hydroxide solutions at 22 ± 1 °C. Unless otherwise specified, the concentrations of all solutions are kept constant at $[FeCl_3]$ = 0.84 M, $[FeCl_2]$ = 0.42 M, $[NH_4OH]$ = 0.70 M and $[Na_2SiO_3]$ = 2.0 M. A glass capillary (length = 27 mm, inner diameter = 1.1 mm) is used to deliver the iron solution into a cylindrical glass vessel (height ≈ 90 mm, inner diameter = 32 mm) containing the silicate–ammonia solution (pH = 13.5). The flow rate of the injected solution is controlled by a syringe pump (KD Scientific 200) and varied between 10 and 35 mL/h. A single tube starts to grow once the injected solution leaves the upper end of the glass capillary. Instantly, the growing tube is pinned to a hollow glass rod (length = 24 cm, inner diameter = 4.0 mm) which is centered in the middle of the glass cylinder and positioned 3–5 mm above the glass capillary. Pinning is achieved through an air bubble which is created using an air-filled syringe and held at the lower end of the glass tube. The glass tube moves up vertically at a constant, predetermined speed in the range of 1.5–6 mm/s. The motion is generated by a servo motor/controller system (BLM-N23-50-1000-B, CDS-3310, Galil). Using this setup, the speed of pinning glass rod dictates the speed at which the forming tube grows upward.

We utilize a charge-coupled device camera (COHU 2122) to acquire optical micrographs of the forming tubes during synthesis. The camera signal is digitized at a typical rate of 4 frames/s by a frame grabber board (DT 3155, Data Translation) and HL Image ++97 software. More details concerning the experimental setup can be found in ref 20. For further characterization, we remove the structures from the silicate solution. Then they are washed three to four times with water until a neutral pH is reached and dried overnight at ambient conditions. The dried tubes are ground into powder (except for SEM and Raman).

2.3. Characterization. We record SEM micrographs on a JEOL JSM-5900 scanning electron microscope coupled with an energy dispersive X-ray spectrometer (EDS) at an acceleration voltage of typically 30 kV. TEM images are obtained on a JEOL 2010 transmission electron microscope operating at 200 kV. Powder X-ray diffraction (PXRD) is carried out at room temperature on Rigaku DMAX 300 Ultima 3 diffractometer using Cu Kα (λ = 1.5418 Å). We estimate the average crystallite size using the Debye–Scherrer equation, $\Delta(2\theta) = 0.9\ \lambda/(s\ \cos(\theta_0))$. Raman spectra are collected at room temperature using a micro Raman system which couples an Olympus BX31 optical microscope to a Horiba Jobin Yvon LabRam HR800 spectrograph with a charge-coupled device detector. The spectra are measured with an Ar^+ laser using the 488 nm line, a laser power of 0.03 mW, and an exposure time of 1 h. ^{57}Fe Mössbauer spectra are performed at 4.5 and 300 K using a conventional constant acceleration transmission spectrometer equipped with a ^{57}Co(Rh) source.

We collect magnetic data on a Quantum Design MPMS XL7 SQUID magnetometer. Field-dependent magnetization data are measured between −7 and +7 T. Zero-field-cooled (ZFC) and Field-Cooled (FC) data are obtained for dc-susceptibility. The ac-susceptibility is measured between 1 and 1000 Hz. Our specific heat measurements are performed on a Quantum Design Physical Property Measurement System.

3. RESULTS

In initial experiments, we prepared iron oxide–silica tubes using 1 M sodium silicate solution in the presence and absence of ammonium hydroxide solution. These tubes lacked mechanical stability and always disintegrated into small fragments during the drying process. Different drying techniques including drying at ambient conditions, vacuum drying, freeze-drying, drying under nitrogen gas, and heat-drying were employed. All these techniques failed to prevent the formed structures from collapsing. This problem was not encountered for copper hydroxide–silica tubes prepared under the same experimental conditions[20] and must be attributed to the high acidity of the injected solution reducing iron precipitation.[21] This problem was resolved by increasing the sodium silicate concentration to 2.0 M. Tubes obtained under these conditions dry without breaking. Nonetheless, the dried tubes are still more fragile than their copper hydroxide–silica counterparts.[20]

Figure 2a shows the X-ray diffraction pattern of the tube material. We find eight peaks, each labeled by the corresponding Miller index, which are in good agreement

dx.doi.org/10.1021/ja3064843 | J. Am. Chem. Soc. 2012, 134, 15519–15527

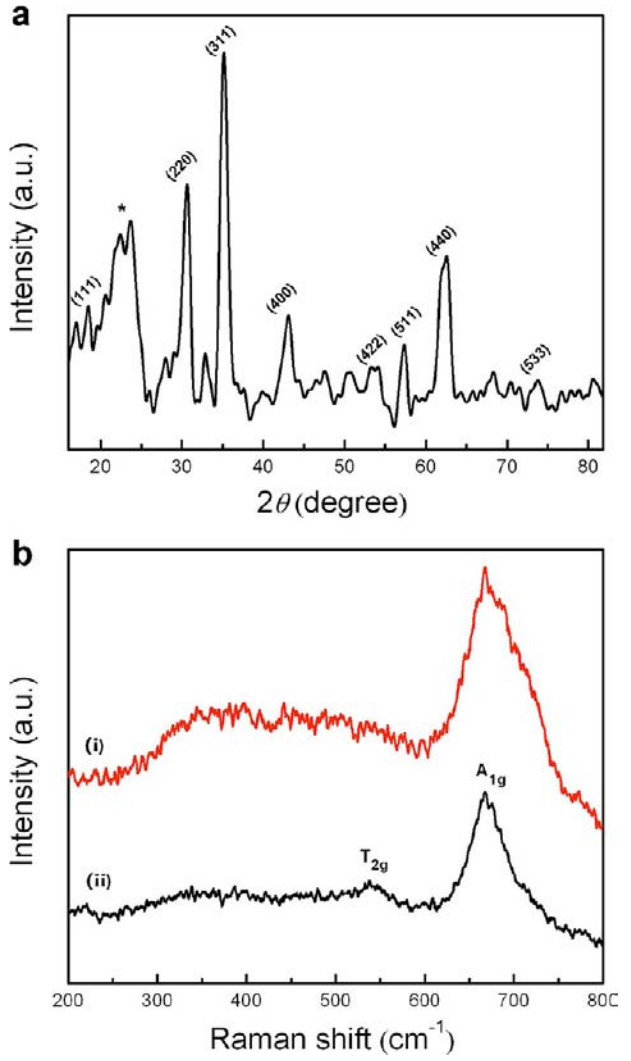

Figure 2. (a) Powder X-ray diffraction pattern of a tube sample obtained for a rod velocity of 3 mm/s and a flow rate of 10 mL/h. (b) Raman spectra of (i) a tube sample (rod velocity, 3 mm/s; flow rate, 22 mL/h) and (ii) a magnetite standard.

with the published magnetite pattern (JCPDS No. 19-0629). The broad feature in the region around 23° (labeled by a star) is assigned to amorphous silica. The average crystallite size calculated from the (311) peak using the Scherrer equation is 7.5 nm. However, since magnetite (Fe_3O_4) and maghemite (γ-Fe_2O_3) have the same spinel structure and similar lattice parameters, it is difficult to distinguish between them solely on the basis of ordinary XRD patterns.[22]

Raman spectroscopy presents a useful tool to overcome this limitation.[22] Figure 2b shows a representative Raman spectrum of the prepared tubes and of a reference sample containing magnetite only. The Raman spectrum of the latter sample exhibits two characteristic bands at 668 cm^{-1} (A_{1g}) and 538 cm^{-1} (T_{2g}), which are fully consistent with the values of magnetite reported in literature.[23] The tube sample shows only one magnetite-characteristic band centered at around 668 cm^{-1}, while none of the maghemite-characteristic peaks (720, 500, and 350 cm^{-1})[22] are observed. The missing 538 cm^{-1} band is probably obscured by amorphous silica present in the sample.[24]

To ascertain the nature of the iron oxide phase and to obtain further information about the distribution of the cations, we performed Mössbauer spectroscopy on the tubes. Figure 3 shows the Mössbauer spectra obtained at 4.5 and 300 K in the absence of an external magnetic field. At 300 K, the sample displays a central doublet with no hyperfine splitting indicating superparamagnetic behavior. The obtained values, summarized in Table 1, are similar to those observed for typical superparamagnetic magnetite nanoparticles.[25,26] At 4.5 K, the spectrum consists of two resolved sextets and no paramagnetic component is observed. The collected parameters are in good agreement with the values reported for magnetite at this temperature.[27−29] The sextet with the higher hyperfine field is attributed to the high spin Fe^{3+} ions in the tetrahedral *A* sites of spinel magnetite and the sextet with the lower hyperfine field is associated with Fe^{2+}/Fe^{3+} ions in the octahedral *B* sites. We note that the isomer shift value observed for the sextet associated with the *B* site (δ = 0.45 mm/s) is lower than that reported for bulk magnetite (δ = 0.67 mm/s).[27,28] This finding indicates the formation of nonstoichiometric magnetite,[30] which is also confirmed by computing the ratio of the *A*-site area to the *B*-site area leading B/A = 1.22 (the relative subspectral area for stoichiometric magnetite is B/A = 2).[23,27]

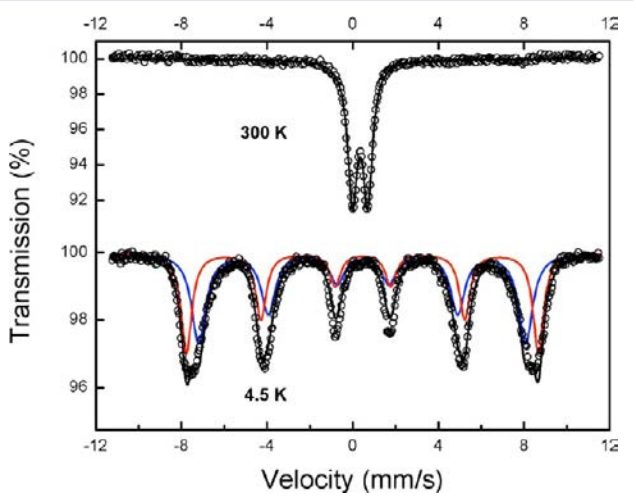

Figure 3. Mössbauer spectra of a representative tube sample recorded at 300 and 4.5 K. During the synthesis of this sample, the rod velocity and the flow rate were 2.5 mm/s and 16 mL/h, respectively.

Table 1. ^{57}Fe Mössbauer Parameters Obtained at 300 and 4.5 K: Isomer Shift (δ), Linewidth (Γ), Quadrupolar Splitting (QS), Hyperfine Field (H), and Spectral Area

T (K)	δ (mm/s)	Γ (mm/s)	QS (mm/s)	H (T)	area (%)
300	0.34	0.27	0.72	–	100
4.5 *A*	0.46	0.30	0.02	51.2	45
4.5 *B*	0.45	0.40	0.04	47.5	55

In a recent report,[20] we have shown that the growth zone for similarly prepared copper hydroxide−silica tubes is located either at the air bubble or at the tube's base (i.e., close to the solution-delivering glass capillary). This behavior depends on the velocity of the glass rod and the flow rate of the injected solution. In the present study, we limited these experimental parameters to the range that ensures growth at the air bubble only. Figure 4 shows two snapshots from a representative experiment where image frame (b) is recorded 4.25 s after

dx.doi.org/10.1021/ja3064843 | J. Am. Chem. Soc. 2012, 134, 15519−15527

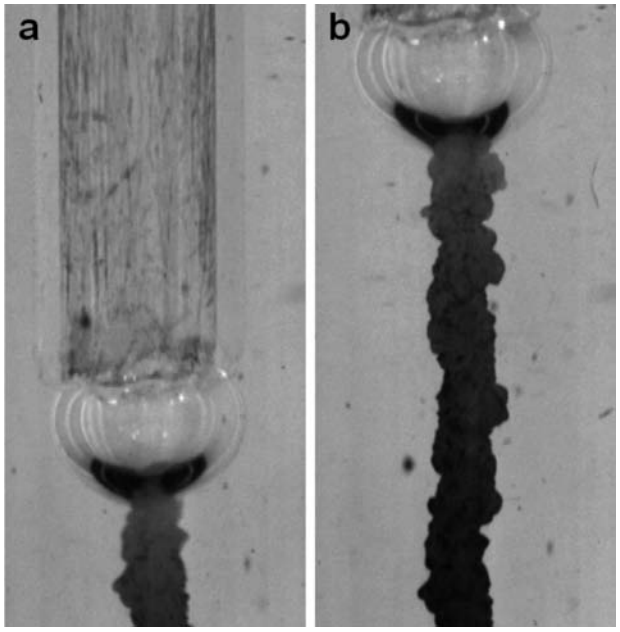

Figure 4. Tube formation imaged by a stationary video camera. Time interval between the two snapshots is 4.25 s. Field of view: 7.1 × 14.6 mm^2. The flow rate of the injected iron (II/III) solution is 10 mL/h and the velocity of the glass rod is 2 mm/s.

frame (a). Notice that these images are recorded using a stationary camera which monitors only a small range of the reaction vessel. As shown in Figure 4, the glass rod and the pinning air bubble move vertically up forming a nearly straight tube in their wake. The radius of the formed tube is not constant but varies in the range of 0.57−0.82 mm with an average radius of r_{exp} = 0.74 mm. This value is very close to the one expected based on volume conservation of the injected solution (r_{cal} = 0.67 mm). The observed nonuniformity in the tube radius could be related to the crystalline nature of the formed magnetite.

Careful inspection of Figure 4b shows a gradual darkening and an increasing opacity of the tube with increasing distances from the bubble. These changes must stem from chemical and/or physical processes within the tube wall and are likely caused by the continuous nucleation and/or growth of magnetite crystals. Figure 5a illustrates these variations in terms of an image intensity profile. For this analysis, we evaluate a rectangular area (width = 0.57 mm, length = 10.84 mm) just below the air bubble. Each data point represents the average intensity of the tube at a certain distance from the bubble. The plot clearly indicates that the intensity decreases with increasing distances from the bubble. Moreover, the data are well described by an exponential decay function of the form

$$I(x) = a + b\, e^{-k_x x} \quad (1)$$

with a decay constant k_x = 0.16 mm^{-1}. The parameters a and b are additional fitting constants that depend strongly on the applied illumination and the detector.

In addition, data from the same experiment are analyzed to investigate the time variation of the intensity at a fixed position. Results are shown in Figure 5b for x = 0.5 mm and x = 2.5 mm. Notice that x denotes the distance of the analyzed position to the lower end of the frame and t_0 is the instant at which the tube wall material starts to form at x = 0.5 mm. Each data point

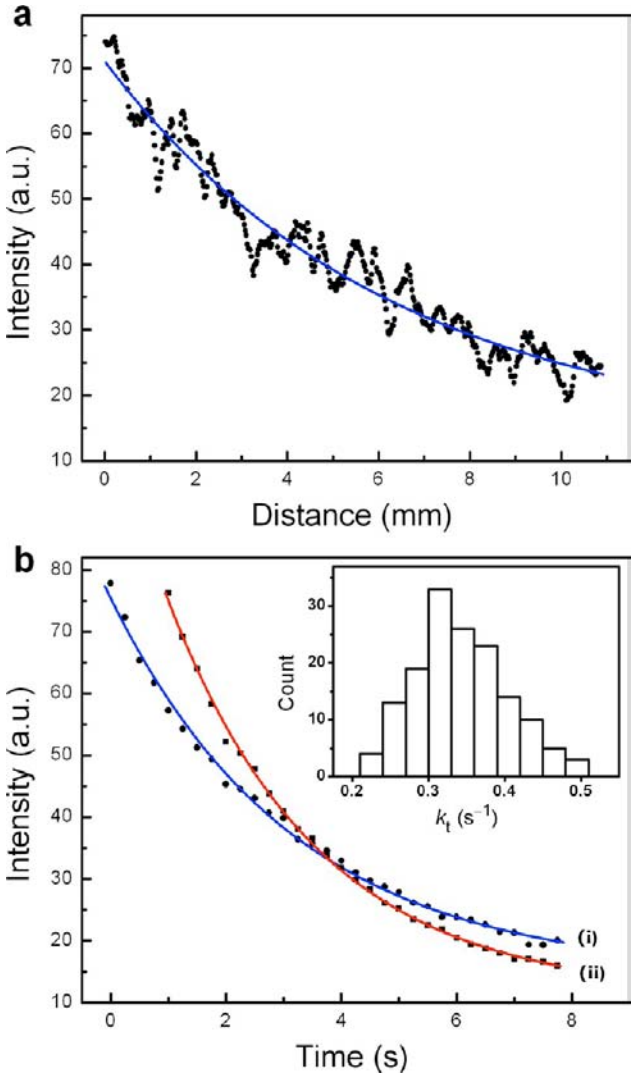

Figure 5. (a) Variation of the intensity along the tube sample shown in Figure 4b. Closed circles represent the average intensity at a certain distance from the air bubble. The solid curve is the exponential fit of lowest root-mean square deviation. (b) Time-intensity plots at x = 0.5 mm (i) and x = 2.5 mm (ii). The continuous curves are the corresponding exponential fits. The inset is the probability distribution of k_t.

represents the average intensity at a certain time t while the continuous curves are corresponding exponential fits using

$$I(t) = c + de^{-k_t t} \quad (2)$$

For the examples in Figure 5b, we find the rate constants k_t = 0.31 s^{-1} and k_t = 0.38 s^{-1} for x = 0.5 and 2.5 mm, respectively. This analysis is repeated for 150 different positions and yields the histogram in the inset of Figure 5b. The distribution is only slightly asymmetric (skewness of 0.35) and yields an average rate constant of k_t (average) = 0.34 s^{-1} and a standard deviation of 0.06 s^{-1}.

The relation between the rate constant k_t and the decay constant k_x can be easily understood as a direct consequence of the steady motion of the tube forming reaction zone. Since this motion is directly controlled by the motion of the glass rod, which obeys x = −2 mm/s t + x_0, the two constants should satisfy the equation

dx.doi.org/10.1021/ja3064843 | J. Am. Chem. Soc. 2012, 134, 15519−15527

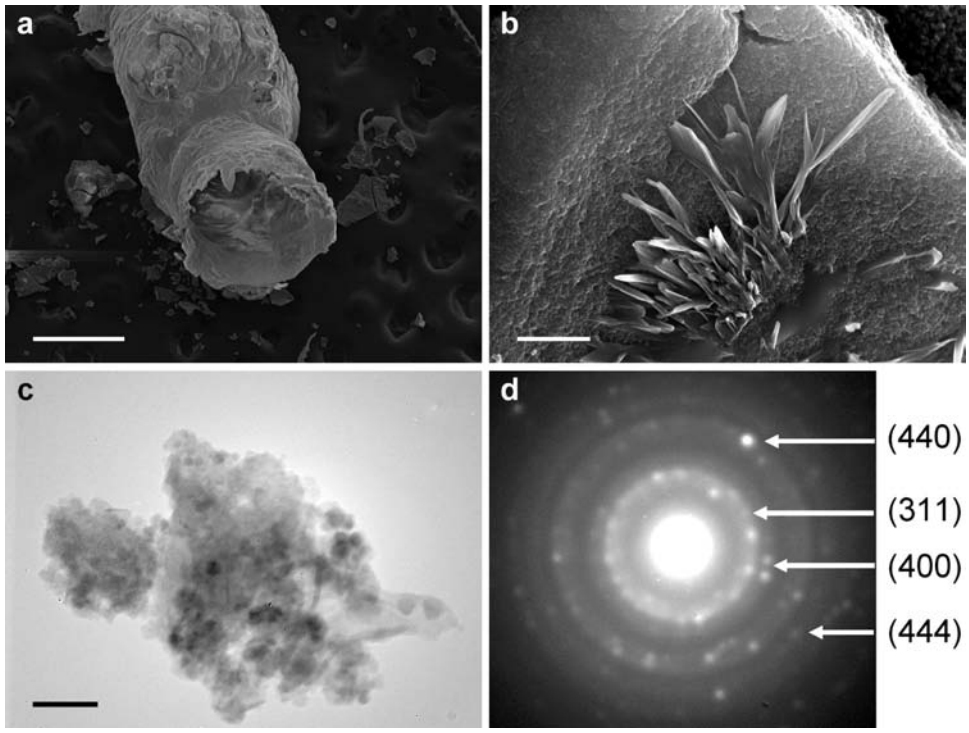

Figure 6. (a) Scanning electron micrograph (SEM) showing the hollow cross section and the outer surface morphology of a formed tube (rod velocity, 5 mm/s; flow rate, 10 mL/h). (b) SEM image revealing distinct magnetite patterns on the inner surface of a tube (rod velocity, 3 mm/s; flow rate, 25 mL/h). (c) TEM image of a tube fragment showing nanocrystals (rod velocity, 3 mm/s; flow rate, 10 mL/h). (d) SAED pattern and corresponding Miller indices. Scale bars: 500 μm (a), 5 μm (b), 50 nm (c).

$$k_x(\mathrm{mm}^{-1}) = k_t(\mathrm{s}^{-1})/(2\ \mathrm{mm/s}) \quad (3)$$

and indeed we find a good agreement with a deviation of 6%.

The time variation of the intensity and in particular the distribution of rate constants could provide interesting details on the growth kinetics of magnetite crystals in this far-from-equilibrium system. However, additional characterization techniques will be required to relate such optical data to the quantitative growth, nucleation, and possibly aggregation dynamics of the nanocrystals.

To obtain further insights into the morphology of the product tubes and the size of their magnetite crystallites, we imaged numerous samples using electron microscopy. Figure 6a is a scanning electron micrograph showing the cross-section of a typical tube. It supports our so far undocumented statement that the tubes are hollow and also documents that tubes remain hollow after drying. The tube has a nonuniform radius and the outer surface appears more rugged than the inner one. However, careful inspection of the latter reveals the formation of polygonal, plate-like segments separated by microsized cracks (see Figures S1a and S1b). The presence of these cracks is a possible explanation of the increased fragility observed for magnetite tubes. We note that similar crack patterns were observed in microshells produced in the reaction of copper sulfate-loaded gel beads with sodium silicate solution.[31] The ruptured shells, however, always "self-healed" during the course of the reaction. The causes for this difference are unknown but might be related to the absence or shorter lifetime of a colloidal gel membrane in the (seemingly more crystalline) magnetite system.

At higher magnification (Figure 6b), we observe distinct leave-like patterns. Each "leaf" has a length in the range of 5−20 μm, a width of approximately 1−2 μm, and a submicrometer thickness. Spectroscopic techniques indicate that the pattern contains iron and is not an artifact due to carbon coating during sample preparation (see Figures S1c and S1d). Figure 6c is a representative TEM image showing particles with a mean diameter in the range of 5−15 nm. This finding is in agreement with the crystallite size computed from the Scherrer equation. The electron diffraction pattern (Figure 6d) has four rings that can be indexed to the magnetite structure.

Figure 7 shows the hysteresis loops of a typical sample measured at two different temperatures. The coercivity (H_c) at 3 K is 460 ± 10 Oe but vanishes at 298 K (see inset of Figure 7). This is a typical superparamagnetic behavior which is expected if the average size of the obtained particles is compared to the theoretical value for the monodomain size of magnetite (~25 nm).[32] Another remarkable aspect of the $M(H)$ curves is that the magnetization does not saturate even at a high applied field of 70 kOe. Hence in the following discussions, we denote the magnetization at 70 kOe as the saturation magnetization (M_s). The values obtained for the latter are 20.2 and 10.5 emu/g at 3 and 298 K, respectively. Assuming the tubes' weight is equally divided between magnetite and silica,[21] this yields saturation magnetizations of 40.4 and 21.0 emu/g of magnetite at 3 and 298 K, respectively. These values are still much lower than the value reported for bulk magnetite (92 emu/g).[33] This reduction is often observed in magnetic nanoparticles and attributed to surface contributions and especially spin canting.[23,25]

Zero-field-cooled (ZFC) and field-cooled (FC) dc susceptibility data are recorded between 2 and 300 K under an applied magnetic field of 200 Oe. The corresponding magnetization curves, shown in Figure 8, coincide at high temperatures but diverge below ~170 K indicating either superparamagnetic or spin-glass behavior. The ZFC curve shows a broad maximum at

dx.doi.org/10.1021/ja3064843 | J. Am. Chem. Soc. 2012, 134, 15519−15527

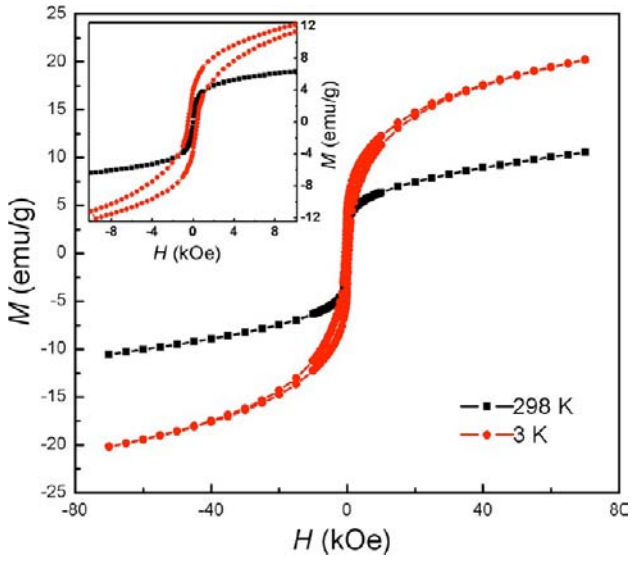

Figure 7. Magnetization curves measured at 3 and 298 K. [$FeCl_3$] = 1.00 M. [$FeCl_2$] = 0.50 M. Rod velocity: 2 mm/s. Flow rate: 10 mL/h. The inset shows a magnified view of the low field region.

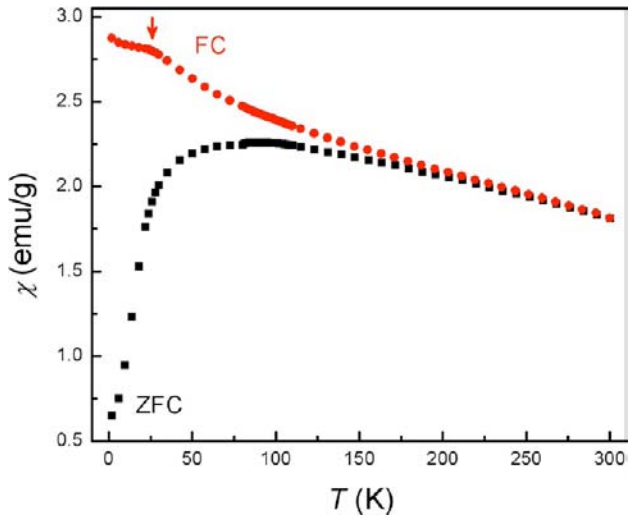

Figure 8. Zero-field-cooled (ZFC) and field-cooled (FC) magnetic susceptibilities in an external magnetic field H = 200 G. Rod velocity: 3 mm/s. Flow rate: 10 mL/h. The arrow indicates the position of the Verwey transition.

~95 K which corresponds to the average blocking temperature T_B of the particles. The broad cusp at T_B indicates a distribution in particle sizes.[34]

The FC curve exhibits a small kink, indicated by an arrow, at $T \sim 20$ K which is not observed in the ZFC curve. The existence of this kink is most likely related to the Verwey transition which is characteristic of magnetite and widely used to distinguish magnetite from maghemite.[28] The transition usually appears at 120 K for bulk stoichiometric magnetite, however several studies have reported the shift of the Verwey transition to lower temperatures due to nonstoichiometry[35] and size effects.[25] To confirm the nature of the observed transition, we performed heat capacity measurements on the obtained tubes. The collected data, shown in Figure 9, indicate no clear anomaly for the whole range of temperatures studied (2−200 K). However, careful inspection of the results reveals the presence of a shoulder-like feature, indicated by an arrow, at T

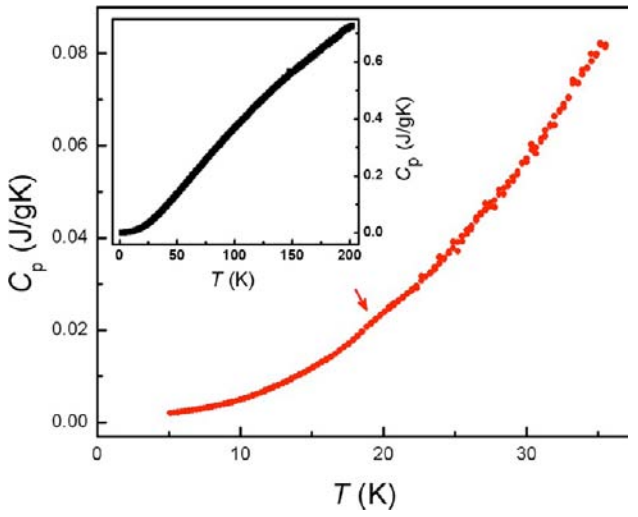

Figure 9. Heat capacity of the tube sample shown in Figure 8. The arrow indicates the position of the Verwey transition. The inset shows the heat capacity measured over a wide temperature range (2−200 K).

~ 20 K which is the same temperature for which we observed the kink in the FC curve. The absence of an obvious anomaly has also been recently noted by Snow et al. who measured the heat capacity of 13 nm magnetite nanoparticles in the temperature range of 0.5−350 K.[36] In their study, however, they found unusual thermal behaviors between 50 and 90 K. The authors showed that the heat capacity in the aforementioned range depends on the cooling rate and time; a behavior that is usually associated with transitions.[36]

To gain more insights into the magnetic properties of the system and to distinguish between superparamagnetic and spin-glass behavior, we measured the temperature-dependent ac-susceptibility. Figure 10 shows the real $\chi'(T)$ and imaginary $\chi''(T)$ components for different frequencies (ν = 1, 10, 100, 1000 Hz) at H_{AC} = 5 Oe. Both components exhibit frequency-dependent behavior and the peak of $\chi''(T)$ shifts to higher temperatures with increasing frequency.

Since there is no clear anomaly of $\chi'(T)$ and because of the broad maximum of $\chi''(T)$, we use the temperature T_i at which the real part $\chi'(T)$ shows an inflection point to estimate the shift of the ac susceptibility as a function of the frequency (see the inset in Figure 10a).[37,38] From the maximal shift ΔT_i, we obtain the value of $\varphi = \Delta T_i/T_i\, \Delta(\log \nu) \approx 0.061$ which is close to the average value of 0.1 reported for superparamagnetic systems.[25,39] The slight difference is believed to originate from interparticle interactions.[40]

The energy barrier for spin relaxation E_a can be obtained by fitting the experimental data to the Arrhenius equation, $\ln(\tau/\tau_0) = E_a/(k_B T)$, where τ is the average relaxation time corresponding to the frequency of the ac measurement, τ_0 is the pre-exponential factor, and k_B is the Boltzmann constant. The plot, shown in Figure 10c, yields E_a = 689 K (0.059 eV) and $\tau_0 = 1.42 \times 10^{-12}$ s. The latter value is close to the typical range of relaxation times reported for superparamagnetic materials (10^{-9} to 10^{-11} s).[25,41]

Finally, we discuss the dependence of the tubes' magnetic properties on the flow rate of the injected iron (II,III) solution Q and the velocity of the glass rod v. For these studies, the concentrations of all reactants (i.e., in the injected solution and in the reservoir solution) are kept constant. Notice that the control parameters Q and v are not of a direct chemical nature

dx.doi.org/10.1021/ja3064843 | J. Am. Chem. Soc. 2012, 134, 15519−15527

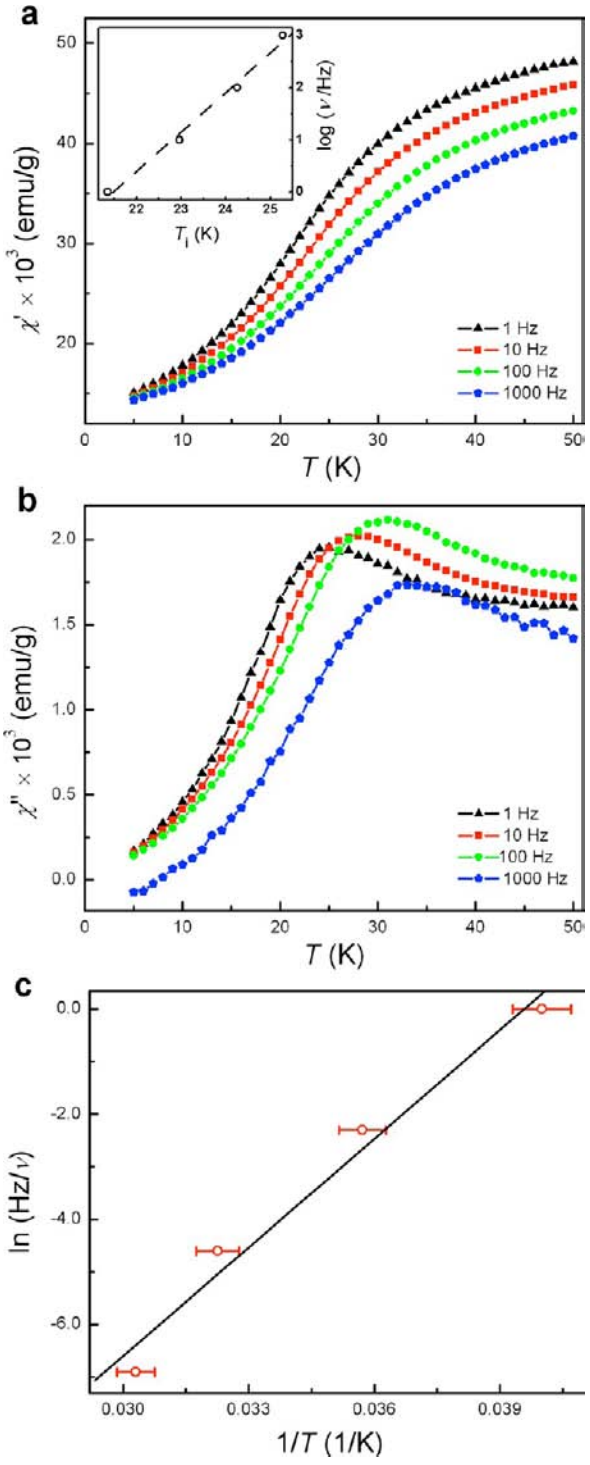

Figure 10. Temperature-dependent ac-susceptibility (1−1000 Hz) data for the tube sample shown in Figure 8. (a) Real part $\chi'(T)$. (b) Imaginary part $\chi''(T)$. (c) Arrhenius plot for the imaginary part $\chi''(T)$. The inset in (a) shows the frequency shift of the inflection point of the real part versus temperature.

but rather mechanical quantities and as such not present, or at least not accessible, in the conventional synthesis of magnetite.[42]

The magnetic properties were measured at T = 3 K. Since this temperature is below T_B, the spins in the magnetite particles are blocked. The flow rate is varied in the range of 10−35 mL/h at a constant rod speed of 3 mm/s, while the rod speed is varied in the range of 1.5−6 mm/s at a constant flow rate of 16 mL/h. Our results are summarized in Figure 11

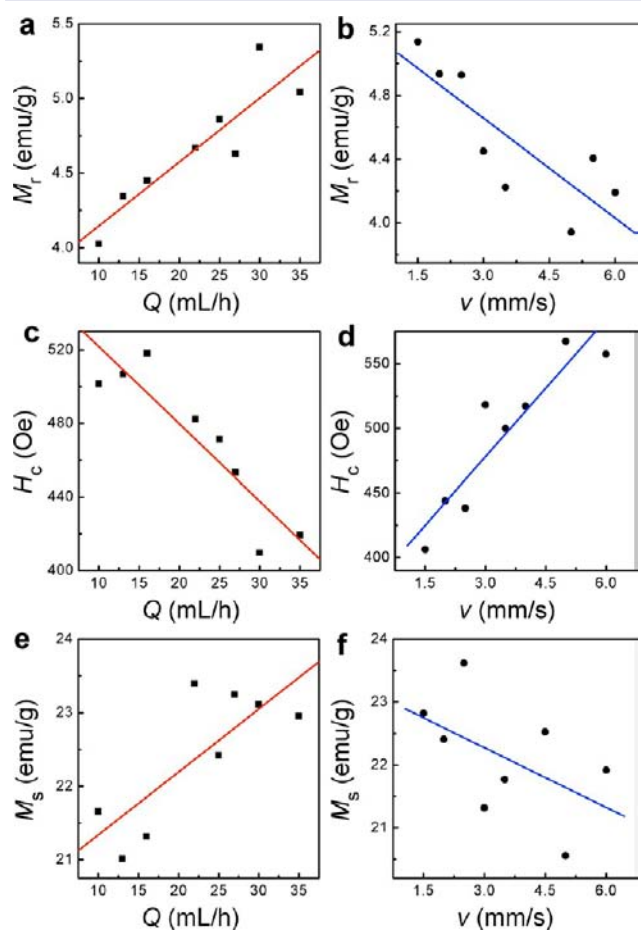

Figure 11. Dependence of the magnetic properties of the formed tubes (remanent magnetization M_r, coercivity H_c, and saturation magnetization M_s) on the rod velocity v and the flow rate Q. The magnetic properties are measured at T = 3 K. v = 3 mm/s (a, c, e) and Q = 16 mL/h in (b, d, f).

where solid markers denote the measured values and the continuous lines represent the results of corresponding linear regressions. Within the experimental error and for the parameter intervals studied, our data show that the saturation magnetization M_s and the remanent magnetization M_r increase with an increase in flow rate and decrease with increasing rod velocity. The coercive field H_c follows exactly the opposite trend; that is, it decreases with an increase in flow rate and increases with increasing rod velocity.

In additional experiments, we studied the variation of the magnetic properties along the length of the formed tubes. These measurements were motivated by the possibility that the systematic trends shown in Figure 11 are caused by reaction-induced, and hence height dependent, changes in iron concentrations within the forming tube. However, no systematic dependence was observed (see Figure S2). This finding indicates, at least for tube lengths of not more than 6.5 cm, a macroscopically uniform distribution of magnetite particles along the formed tubes as well as uniform magnetic characteristics.

While our experimental approach differs significantly from prior methodologies, its results can be discussed in terms of

dx.doi.org/10.1021/ja3064843 | J. Am. Chem. Soc. 2012, 134, 15519−15527

earlier studies regarding size-dependent changes in the magnetic properties of magnetite particles. For instance, Dutta et al. investigated the oleic acid/oleylamine coated magnetite nanoparticles in a size range of 4−12 nm.[43] The authors showed that the saturation magnetization decreases while the coercivity increases as the diameter of the magnetite particles decreases. The authors attributed this result to an increased contribution of disordered surface spins for small particles (core−shell model).[43] More recently, Khosroshahi and Ghazanfari reported an increase in the saturation magnetization and a decrease in the coercivity for increasing sizes of silica coated magnetite nanoparticles.[44] These analogies strongly suggest that the trends observed in Figure 11 stem from a size dependence of the magnetite particle on the growth-controlling parameters. More specifically, they indicate an increase in the size of the magnetite particles with increasing flow rate and/or decreasing rod velocity. The latter result is quite surprising and important as it suggests that the size of magnetite particles (and hence the tubes' magnetic properties) can be controlled by adjusting the mechanical parameters that control the macroscopic structure. One can further speculate that these size differences are caused by reaction-transport induced pH changes as such a dependence has been discussed by Aona et al. in a study that compared reverse and normal coprecipitation methods.[45] However, more work is needed to support such a conclusion.

4. CONCLUSION

In summary, we have developed an externally controlled method for the formation of millimeter-scale magnetite−silica tubes under nonequilibrium conditions. The far-from-equilibrium character of our synthesis manifests itself in steep gradients for all reactant concentrations. Notice that in conventional methods such gradients would swiftly decay due to diffusion; here, however, they are stationary within a steadily moving, self-organized reaction zone. Furthermore, we control the diameter and the velocity of this, ring-shaped zone through two mechanical parameters. The product structures are superparamagnetic at room temperature and show evidence for the Verwey transition at 20 K. In addition, the magnetite nanoparticles obey first-order kinetics with a final size in the range of 5−15 nm.

Perhaps the most important result of our study is that not only the tubes' macroscopic features, but also their nanoscopic and magnetic properties depend systematically on the employed flow rate and rod velocity (Figure 11). This surprising finding establishes additional control over the synthesis of the magnetite particles which could allow for numerous interesting applications. For instance, it should be possible now to produce particles with tailored, arbitrary size distributions simply by selecting appropriate time-dependent rod velocities. Furthermore, it should be possible to spatially unfold these size distributions, thus creating intricate patterns of nanoscale objects on the supporting silica matrix. In addition, it seems reasonable to assume that the microscopic and macroscopic features of the magnetite−silica tubes are susceptible to externally applied magnetic fields during their production.[46]

It is also likely that our approach can be extended to support other systems such as carbonates, borates, or phosphates as well as to other nanoparticles. This prediction is supported by the close similarity between our system and the so-called "chemical (or silica) gardens" in which tube growth is initiated in various solutions and from crystals, polycrystalline aggregates, or pellets of various (not group I) metal salts.[47−49] In this context, we point out that—to our knowledge—this study is the first demonstration of tube formation from cationic reactants that are not a pure substance but a solution of several compounds. Clearly more work is needed to explore the broad possibilities that arise from the different, novel aspects of our study.

■ ASSOCIATED CONTENT

Supporting Information

Representative movie (avi) of the tube growth dynamics, SEM micrographs showing crack formation and additional details about tube morphology and composition. This material is available free of charge via the Internet at http://pubs.acs.org.

■ AUTHOR INFORMATION

Corresponding Author

steinbck@chem.fsu.edu

Notes

The authors declare no competing financial interest.

■ ACKNOWLEDGMENTS

This work is supported by the National Science Foundation under Grant No. 1005861. TEM, Mössbauer and heat capacity data are collected at the National High Magnetic Field Laboratory which is funded by the NSF, the State of Florida and the DOE. We thank Drs. Andrew Ozarowski, Haidong Zhou, Yi-Feng Su and Eric Lochner for assistance.

■ REFERENCES

(1) Mann, S.; Ozin, G. A. *Nature* **1996**, *382*, 313.
(2) Cölfen, H.; Mann, S. *Angew. Chem., Int. Ed.* **2003**, *42*, 2350.
(3) Pojman, J. A.; Ilyashenko, V. M.; Khan, A. M. *J. Chem. Soc., Faraday Trans.* **1996**, *92*, 2825.
(4) White, S. R.; Sottos, N. R.; Geubelle, P. H.; Moore, J. S.; Kessler, M. R.; Sriram, S. R.; Brown, E. N.; Viswanathan, S. *Nature* **2001**, *409*, 794.
(5) Maselko, J.; Borisova, P.; Carnahan, M.; Dreyer, E.; Devon, R.; Schmoll, M.; Douthat, D. *J. Mater. Sci.* **2005**, *40*, 4671.
(6) Collins, C.; Zhou, W.; Mackay, A. L.; Klinowski, J. *Chem. Phys. Lett.* **1998**, *286*, 88.
(7) Van Bommel, K. J.; Friggeri, A.; Shinkai, S. *Angew. Chem., Int. Ed.* **2003**, *42*, 980.
(8) Yan, C.; Liu, J.; Liu, F.; Wu, J.; Gao, K.; Xue, D. *Nanoscale Res. Lett.* **2008**, *3*, 473.
(9) Chopra, N. G.; Luyken, R. J.; Cherrey, K.; Crespi, V. H.; Cohen, M. L.; Louie, S. G.; Zettl, A. *Science* **1995**, *269*, 966.
(10) Jia, C.; Sun, L.; Yan, Z.; You, L.; Luo, F.; Han, X.; Pang, Y.; Zhang, Z.; Yan, C. *Angew. Chem., Int. Ed.* **2005**, *44*, 4328.
(11) Ritchie, C.; Cooper, G. J. T.; Song, Y.-F.; Streb, C.; Yin, H.; Parenty, A. D. C.; MacLaren, D. A.; Cronin, L. *Nature Chem.* **2009**, *1*, 47.
(12) Cooper, G. J. .; Cronin, L. *J. Am. Chem. Soc.* **2009**, *131*, 8368.
(13) Cooper, G. J. T.; Boulay, A. G.; Kitson, P. J.; Ritchie, C.; Richmond, C. J.; Thiel, J.; Gabb, D.; Eadie, R.; Long, D.-L.; Cronin, L. *J. Am. Chem. Soc.* **2011**, *133*, 5947.
(14) Chen, B.; Xu, Q.; Zhao, X.; Zhu, X.; Kong, M.; Meng, G. *Adv. Funct. Mater.* **2010**, *20*, 3791.
(15) Mohapatra, S. K.; Misra, M.; Mahajan, V. K.; Raja, K. S. *Mater. Lett.* **2008**, *62*, 1772.
(16) Pagano, J. J.; Bánsági, T.; Steinbock, O. *Angew. Chem., Int. Ed.* **2008**, *47*, 9900.
(17) Collins, C.; Mokaya, R.; Klinowski, J. *Phys. Chem. Chem. Phys.* **1999**, *1*, 4669.

(18) Stone, D. A.; Goldstein, R. E. *Proc. Natl. Acad. Sci. U.S.A.* **2004**, *101*, 11537.
(19) Parmar, K.; Chaturvedi, H. T.; Akhtar, M. W.; Chakravarty, S.; Das, S. K.; Pramanik, A.; Ghosh, M.; Panda, A. K.; Bandyopadhya, N.; Bhattacharjee, S. *Mater. Charact.* **2009**, *60*, 863.
(20) Makki, R.; Steinbock, O. *J. Phys. Chem. C* **2011**, *115*, 17046.
(21) Pagano, J. J.; Thouvenel-Romans, S.; Steinbock, O. *Phys. Chem. Chem. Phys.* **2007**, *9*, 110.
(22) Jia, C.-J.; Sun, L.-D.; Yan, Z.-G.; Pang, Y.-C.; You, L.-P.; Yan, C.-H. *J. Phys. Chem. C* **2007**, *111*, 13022.
(23) Daou, T. J.; Pourroy, G.; Bégin-Colin, S.; Grenèche, J. M.; Ulhaq-Bouillet, C.; Legaré, P.; Bernhardt, P.; Leuvrey, C.; Rogez, G. *Chem. Mater.* **2006**, *18*, 4399.
(24) Perriot, A.; Vandembroucq, D.; Barthel, E.; Martinez, V.; Grosvalet, L.; Martinet, C.; Champagnon, B. *J. Am. Ceram. Soc.* **2006**, *89*, 596.
(25) Goya, G. F.; Berquó, T. S.; Fonseca, F. C.; Morales, M. P. *J. Appl. Phys.* **2003**, *94*, 3520.
(26) Mikhaylova, M.; Kim, D. K.; Bobrysheva, N.; Osmolowsky, M.; Semenov, V.; Tsakalakos, T.; Muhammed, M. *Langmuir* **2004**, *20*, 2472.
(27) Murad, E.; Cashion, J. *Mössbauer Spectroscopy of Environmental Materials and Their Industrial Utilization*; Kluwer Academic Publishers: London, 2004.
(28) Cornell, R. M.; Schwertmann, U. *The Iron Oxides: Structure, Properties, Reactions, Occurrence and Uses*; VCH: New York, 1996.
(29) Goya, G. F.; Morales, M. *J. Metastable Nanocryst. Mater.* **2004**, *20*, 673.
(30) Roca, A. G.; Marco, J. F.; Morales, M. P.; Serna, C. J. *J. Phys. Chem. C* **2007**, *111*, 18577.
(31) Makki, R.; Al-Humiari, M.; Dutta, S.; Steinbock, O. *Angew. Chem., Int. Ed.* **2009**, *48*, 8752.
(32) Morel, A. L.; Nikitenko, S. I.; Gionnet, K.; Wattiaux, A.; Lai-Kee-Him, J.; Labrugere, C.; Chevalier, B.; Deleris, G.; Petibois, C.; Brisson, A.; Simonoff, M. *ACS Nano* **2008**, *2*, 847.
(33) Cullity, B. D.; Graham, C. D. *Introduction to Magnetic Materials*; 2nd ed.; Wiley-IEEE Press: Hoboken, NJ, 2008.
(34) Perez, J. A. L.; Quintela, M. A. L.; Mira, J.; Rivas, J.; Charles, S. *J. Phys. Chem. B* **1997**, *101*, 8045.
(35) Aragón, R.; Shepherd, J. P.; Koenitzer, J. W.; Buttrey, D. J.; Rasmussen, R. J.; Honig, J. M. *J. Appl. Phys.* **1985**, *57*, 3221.
(36) Snow, C. L.; Shi, Q.; Boerio-Goates, J.; Woodfield, B. F. *J. Phys. Chem. C* **2010**, *114*, 21100.
(37) Tsurkan, V.; Hemberger, J.; Klemm, M.; Klimm, S.; Loidl, A.; Horn, S.; Tidecks, R. *J. Appl. Phys.* **2001**, *90*, 4639.
(38) Baek, S.; Choi, K.; Reyes, A.; Kuhns, P.; Curro, N.; Ramanchandran, V.; Dalal, N.; Zhou, H.; Wiebe, C. *J. Phys.: Condens. Matter* **2008**, *20*, 135218.
(39) Mydosh, J. A. *Spin Glasses: An Experimental Introduction*; Taylor & Francis: London, 1993.
(40) Goya, G. F. *IEEE Trans. Magn.* **2002**, *38*, 2610.
(41) Zheng, W.; Strouse, G. F. *J. Am. Chem. Soc.* **2011**, *133*, 7482.
(42) Massart, R. *IEEE Trans. Magn.* **1981**, *17*, 1247.
(43) Dutta, P.; Pal, S.; Seehra, M. S.; Shah, N.; Huffman, G. P. *J. Appl. Phys.* **2009**, *105*, 07B501.
(44) Khosroshahi, M. E.; Ghazanfari, L. *Mater. Sci. Eng., C* **2012**, *32*, 1043.
(45) Aono, H.; Hirazawa, H.; Naohara, T.; Maehara, T.; Kikkawa, H.; Watanabe, Y. *Mater. Res. Bull.* **2005**, *40*, 1126.
(46) Duan, W. Y.; Kitamura, S.; Uechi, I.; Katsuki, A.; Tanimoto, Y. *J. Phys. Chem. B* **2005**, *109*, 13445.
(47) Cartwright, J. H. E.; García-Ruiz, J. M.; Novella, M. L.; Otálora, F. *J. Colloid Interface Sci.* **2002**, *256*, 351.
(48) Glaab, F.; Kellermeier, M.; Kunz, W.; Morallon, E.; García-Ruiz, J. M. *Angew. Chem., Int. Ed.* **2012**, *51*, 4317.
(49) Makki, R.; Roszol, L.; Pagano, J. J.; Steinbock, O. *Philos. Trans. R. Soc., A* **2012**, *370*, 2848.